# Structural Characterization of 9-Cyanoanthracene−$(Ar)_n$ ($n = 0-3$) by Rotational Coherence Spectroscopy

**Kazuhiro Egashira, Yasuhiro Ohshima,* and Okitsugu Kajimoto†**

*Department of Chemistry, Graduate School of Science, Kyoto University, Kitashirakawa-Oiwakecho, Sakyo-ku, Kyoto 606-8502, Japan*

*Received: September 28, 2000; In Final Form: November 28, 2000*

Rotational coherence spectroscopy implemented with time-resolved fluorescence depletion has been applied in a structural study of 9-cyanoanthracene (CNA) and its clusters with Ar up to three atoms. For bare CNA, *C*-type transients for the $S_1$ and $S_0$ states have been observed separately, yielding independent sets of rotational constants for the two states. For the Ar clusters, rotational constants as averages for $S_1$ and $S_0$ have been derived to fix the cluster geometry. The Ar atom in CNA−Ar is located 3.46 ± 0.03 Å above the central aromatic ring of CNA and displaced slightly from the ring center toward the cyano group. The plane−Ar distance is quite close to those in clusters with other polycyclic aromatic molecules. Two values (∼0.2 or 0.6 Å) for the displacement to the cyano group are consistent with the experimental data, and results on related aromatics−Ar show that the former is preferable. The dominant conformer of CNA−$(Ar)_2$ has been determined as a two-sided (1 + 1)-type: structures for each sides of the CNA plane are the same as that of CNA−Ar within the experimental uncertainties. CNA−$(Ar)_3$ has a (2 + 1)-type structure: one side of the substrate is the same as CNA−Ar, and an Ar dimer lies 3.48 ± 0.04 Å above the other side. The determined conformations of CNA−$(Ar)_{1,3}$ are the same as those of the corresponding anthracene clusters, but that of CNA−$(Ar)_2$ is in contrast to that of anthracene−$(Ar)_2$, which has been identified as a (2 + 0)-type. Model potential calculations have been employed to explain the difference in structural motifs of the two closely related clusters.

## 1. Introduction

Among various solvated clusters containing an aromatic molecule as a chromophore, aromatics−$(rare\ gas)_n$ clusters are characterized by the ultimate simplicity of the solvents that possess no shapes or internal degrees of freedom. This simplicity makes the clusters fairly effective systems to study solute−solvent interactions and their correlation to internal dynamics. For instance, the following issues have been extensively explored for aromatics−$(rare\ gas)_n$ clusters: modification of the electronic character of the chromophore (most frequently studied as size- and site-dependent spectral shifts by solvation),[1−6] multidimensional vibrational dynamics and rigid-fluxional transitions in structure,[7−11] intra- and intermolecular-vibrational energy flow often followed by predissociation of clusters,[12,13] and microsolvation effects on nonradiative dynamics.[1,13,14] To support these studies, considerable efforts have been made to develop reliable models for intermolecular potential-energy surfaces (IPSs). For relatively small systems, e.g., benzene−Ar, quite accurate IPSs have been derived from detailed spectroscopic data[15] or high-level ab initio calculations.[16,17] Such advanced treatments, however, are practically impossible at present for larger systems, and it has been widely adopted to construct empirical IPSs on the basis of rather simple physical concepts.[4,5,7−11,18]

It has been generally accepted that the dispersion term is predominant as the attractive interactions between a rare-gas atom and an aromatic molecule, so that the atom resides exclusively on the aromatic ring of the solute.[4,5,7−11] This has been confirmed by a number of studies on aromatics−Ar clusters by Fourier transform microwave spectroscopy (FTMWS),[19−24] high-resolution laser spectroscopy (HRLS) in the visible and UV region,[25−31] and rotational coherence spectroscopy (RCS).[32−35] As is shown in these studies, Ar has been chosen most frequently as a rare-gas atom because of the convenience in experiments. For $n \geq 2$, the solvent−solvent interaction is also operative, and there are two possible conformations that are so different in a view of the geometrical structure. In the first type of conformation, often termed "wet-type," rare-gas atoms spread on both sides of the aromatic substrate, whereas all rare-gas atoms are gathered on the one side in the other ("nonwet-type") conformation.[8−10] Because a subtle balance in the solute−solvent and solvent−solvent interactions decides whether the aromatic−$(rare\ gas)_n$ cluster of interest shows wetting or nonwetting behavior, the experimental determination of the cluster conformation is a crucial test for model IPSs.

In the respect just mentioned, studies on minimal size ($n = 2$) clusters with different conformations are particularly important, but there have not been so many reports on their structural determination in contrast to those of $n = 1$. Wetting (1 + 1)-type isomers have been identified for *s*-tetrazine−$(Ar)_2$ by HRLS[25] and for furan−$(Ar)_2$ and pyridine−$(Ar)_2$ by FT-MWS.[36,37] [In the notation of ($m + l$)-type, $m$ and $l$ represent the numbers of argon atoms on the two sides of the aromatic substrate.] For benzene−$(Ar)_2$, two series of vibronic bands have been observed and assigned to wetting (1 + 1) and nonwetting (2 + 0) isomers on the basis of their spectral band shifts.[38] The former form has been confirmed by HRLS,[39] but the latter has not so far. The coexistence of the two isomers has also been reported for perylene−$(Ar)_2$,[4] and both of them have been

* To whom correspondence should be addressed. Fax: +81-75-753-3974. E-mail: ohshima@kuchem.kyoto-u.ac.jp.

† Also Core Research for Evolutional Science and Technology (CREST), Japan Science and Technology Corporation (JST).

10.1021/jp0035378 CCC: $20.00 
Published on Web 01/27/2001

confirmed by RCS in this case.[32] For clusters of tricyclic aromatics, i.e., anthracene,[5,10] carbazole,[8] and fluorene,[2] the vibronic spectra for $n = 2$ are dominated by a single isomer. RCS has been applied to the former two species to identify the dominant form of anthracene$-(Ar)_2$ as a $(2 + 0)$-type[33] and that of carbazole$-(Ar)_2$ as a $(1 + 1)$-type.[40] It has also been shown that anthracene$-(Ar)_3$ is of the $(2 + 1)$-type.[33] HRLS has confirmed the result on carbazole$-(Ar)_2$[41] and shown that the structure of fluorene$-(Ar)_2$ is similar.[42] The results on anthracene$-(Ar)_2$ are consistent with those of the model potential calculations,[5,11] but the global minimum of carbazole$-(Ar)_2$ has been predicted also as the $(2 + 0)$ form,[8] which contradicts the experimental observation. This discrepancy clearly shows the necessity for more critical evaluation of the model IPSs by further systematic studies on other aromatics$-$(rare gas)$_n$ clusters with $n \geq 2$.

The experimental methods so far applied to aromatics$-$(rare gas)$_n$ clusters have their own merits and limitations. FTMWS and HRLS can provide fairly accurate spectroscopic data, owing to their high frequency resolution. However, the application to large systems is extremely difficult for the frequency-domain methods, because of spectral congestion and weak intensity, due to small rotational constants and large partition functions, of individual lines. Accordingly, there has been no reports on clusters of polycyclic aromatics by FTMWS, and HRLS studies on clusters with $n \geq 2$ are limited.[25,39,41,42] On the other hand, the time-domain method of RCS is virtually free from such a deficiency, though accuracy of RCS-derived data is often inferior to those from the frequency-domain methods.[43] Thus, RCS is most suitable to the objective of the study presented here, the structural characterization of clusters that contain a tricyclic aromatic molecule solvated with several rare-gas atoms.

In the present paper, we report RCS measurements on 9-cyanoanthracene (CNA) and its clusters with Ar, up to three atoms. Bare CNA in jet-cooled conditions has been well studied in relation to its nonradiative decay process.[14,44] Laser-induced fluorescence spectra of CNA$-(Ar)_n$ were observed for $n = 1-5$,[45] and their spectral shifts were analyzed.[46] However, no experimental information on their geometries has been reported. In the present study, CNA is selected as an anthracene derivative that contains a polar functional group. Substitution of the hydrogen atom at the 9 position by the cyano group will modify the solute$-$solvent interaction to some extent, and it is examined whether this modification results in a detectable difference between the structural parameters of CNA$-(Ar)_n$ and those of the corresponding anthracene clusters. The conformational change from nonwet- to wet-type is experimentally verified for the $n = 2$ cluster. A model potential calculation is performed to estimate the relative stabilities of the two conformations, and the results are compared with the experimental observation.

## 2. Experimental Section

The present RCS experiments were performed by utilizing time-resolved fluorescence depletion (TRFD).[47] The pump and probe pulses for TRFD were produced by a solid-state picosecond laser system. A mode-locked femtosecond Ti:sapphire laser (Spectra Physics, Tsunami) pumped by a 5.0 W diode-pumped continuous wave (CW) Nd:$YVO_4$ laser (Spectra Physics, Millennia) generated an 82 MHz pulse train with the output energy of 0.7 W. The bandwidth of the laser light was more than 10 nm, around 760 nm. This output was amplified by a regenerative amplifier (Spectra Physics, Spitfire) pumped by an 8 W Q-switched Nd:YLF laser (Spectra Physics, Merlin) to generate 0.5 mJ light pulses at a 1 kHz repetition rate. A high-dispersive grating (2200 lines/mm) and a slit mask were installed in the amplifier to reduce the laser bandwidth down to $<1$ nm. The pulse width of the amplified output was $\sim$1 ps full width at half-maximum (fwhm), which was monitored by a single-shot autocorrelator (Positive Light, SSA). After collimated by one-half in diameter, the fundamental of the laser was frequency-doubled in an $LiBO_3$ crystal to produce excitation pulses for transitions of the species to be studied. The second harmonic thus generated was directed through a Michelson interferometer, which consisted of two hollow-reflectors (Newport), to generate pump and variably delayed probe pulses of equal intensity. The probe beam could be delayed in time by a computer-controlled linear-positioning stage (Sigma Koki) with a minimum step size of $\Delta t = 33$ fs. The pump and probe pulse trains, polarized parallel to one another, were recombined and sent collinearly into a vacuum chamber, after further being collimated to $\sim$1 mm in diameter. The pulse trains intersected supersonic free jets perpendicularly at a distance of 5 mm from the expansion orifice ($X/D \approx 70$). The averaged output of the UV light was $\sim$30 $\mu$J/pulse, and its wavelength was monitored with a 0.5 m monochromator (Spex, 500M) coupled with a charge-coupled device detector (CVI, AD150) so as to set on the resonance of the molecules. Its spectral bandwidth was $\sim$0.2 nm in the UV region. The temporal width was estimated to be almost equal to that of the fundamental light.

The clusters of CNA with Ar were formed in supersonic free-jet expansions. CNA, whose melting point is 173$-$177 °C, was vaporized in a sample reservoir directly attached to a CW nozzle, both of which were heated by a sheath heater surrounding them. The temperature of the reservoir was kept around 150 °C. The carrier gas consisted primarily of helium with a small amount of argon, which was mixed in by means of a needle-valve arrangement. It was regulated to be 5 atm and led into the reservoir of CNA. The gas sample containing trace amount of vaporized CNA was expanded continuously into a vacuum chamber through a small orifice (70 $\mu$m in diameter). The temperature of the nozzle, measured with a chromel$-$arumel thermocouple attached on it, was kept at a temperature slightly (about 5 °C) higher than that of the reservoir. The vacuum chamber was evacuated by 10 in. (Edwards, 250/2000M) and 6 in. (ULVAC, ULK-06A) diffusion pumps, which were backed by a mechanical booster pump (Edwards, EH 250) and a rotary pump (Edwards, E2M 80) in series. The base pressure in the chamber was better than $10^{-5}$ Torr. The pressure was maintained at $5 \times 10^{-4}$ Torr in the experiment.

Time-integrated fluorescence was collected using two quartz lenses, filtered with a sharp-cut long-pass filter (Schott, GG 400) to eliminate scattered light from the excitation pulse, and detected with a photomultiplier tube (Hamamatsu, R928) held perpendicularly to the laser and molecular beams. The fluorescence signal was preamplified, filtered by a 1 kHz high-pass filter, and fed into a boxcar integrator (SRS, SR250), whose output was finally stored by a personal computer as a function of the delay between the pump and probe pulses to yield a TRFD trace. A typical completed scan corresponds to the average of some dozens of individual traces, each of which was obtained by averaging 300 laser shots at each delay position (step size 3.3 ps).

Before the RCS measurements, laser-induced fluorescence spectra of the CNA$-(Ar)_n$ clusters were observed using a tunable dye laser (Lambda Physik, SCANmate 2E) pumped by a 10 Hz XeCl excimer laser (Lambda Physik, COMPex 102) to determine the transition frequency of each species and optimize the conditions. The wavelength of the laser was

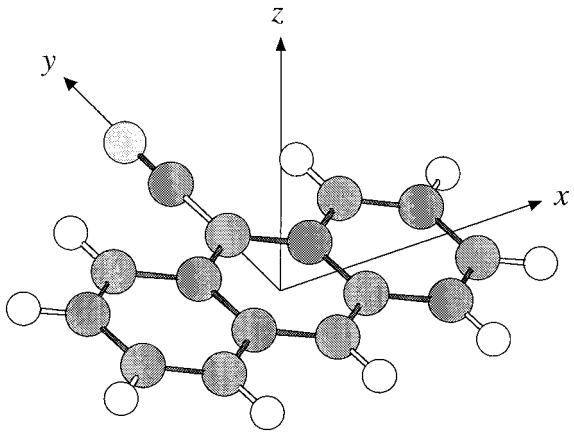


**Figure 1.** CNA with the molecule-fixed axes used herein. The origin of the coordinate system is the center of the central aromatic ring of the molecule.

calibrated with the 0.5 m monochromator. The UV light (bandwidth $<0.5$ cm$^{-1}$) crossed the molecular jet 5 mm downstream of the CW nozzle. Fluorescence was detected and averaged with the same apparatus as that used in the RCS-TRFD experiments.

## 3. Results

To determine the rotational constants from the data, the RCS traces so obtained were compared with simulated ones. The simulations were carried out by using a program, which was coded in accord with the theoretical consideration by Felker and co-workers.[48−50] In short, rotational constants of the species of interest were calculated for its estimated geometry and used to construct rotational Hamiltonian matrices, which were numerically diagonalized to give eigenvalues and eigenvectors for rotational levels. Quantum-beat frequencies and their amplitudes for levels connected by mutually parallel-polarized pump and probe pulses were calculated by using the eigenvalues and eigenvectors. Finally, ensemble averaging of the sinusoidal quantum beats was taken for the thermal (i.e., Boltzmann) distribution of the rotational levels, yielding calculated RCS traces to be compared with the observed ones. For simplicity, the ground-state expression for RCS transients was employed throughout the study, which has been shown to be sufficient to simulate both ground- and excited-state RCS traces.[50] It has also been shown that the widths of transients depend on the inverse square root of the rotational temperature.[50] When the simulations were preformed, the rotational temperature was assumed to be 5 K, for which the widths could be well reproduced. Because the laser pulse duration was much narrower than that of the RCS transients (typically $\geq$20 ps fwhm), convolution was not necessary for simulating the RCS traces.

We define the axis system (denoted as *x*, *y*, and *z*) fixed to the CNA moiety in accord with Pariser's axis-labeling convention, as shown in Figure 1. They direct along with the *a*, *b*, and *c* principal axes, respectively. It is noted that the origin of the axes is set to the center of the central aromatic ring of the CNA molecule in the present definition (not the center of mass of the molecule). For the $0_0^0$ excitation of the $S_1(B_2)-S_0(A_1)$ transition of the CNA monomer, the transition dipole moment lies along the in-plane short (*y* or *b*) axis of the CNA moiety.[51] Even after cluster formation, its direction is assumed to be unchanged in the CNA-fixed axis system. Because the orientation of the principal axis system of the clusters does not necessarily coincide with the that of the CNA-fixed system, the transitions of the clusters may be either of *b*-, *c*-, or hybrid-type. Principal-axis components of the transition dipole moment are evaluated as projections of the vector along the *y* axis.

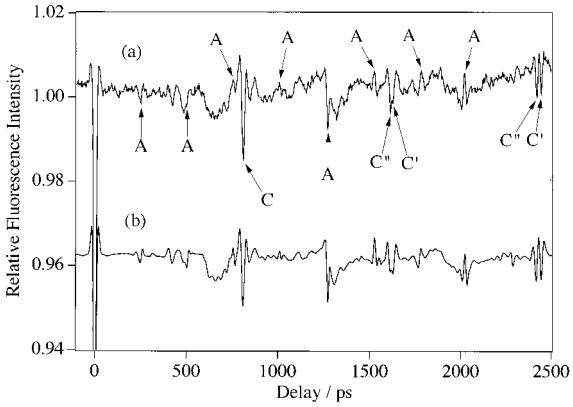


**Figure 2.** RCS traces of bare CNA. (a) Experimental TRFD trace recorded with its $S_1-S_0$ origin band. Features labeled with C's or A's are assigned as *C*- or *A*-type rotational coherence transients. Single and double primes represent signals for the upper and lower states, respectively. (b) Simulated trace, which is calculated as a sum of the $S_0$ and $S_1$ coherences. The *A*, *B*, and *C* constants used are 0.986, 0.452, and 0.310 GHz for $S_0$ and 0.986, 0.446, and 0.307 GHz for $S_1$, respectively. The horizontal scale indicates the relative intensity for the observed fluorescence, and the calculated trace is scaled to be similar to the experimental one.

**TABLE 1: RCS-Derived Rotational Constants of CNA−(Ar)$_n$ ($n$ = 0−3)[a]**

| species | $B+C$ | $2A-B-C$ | $A$ | $C$ |
|---|---|---|---|---|
| CNA | | | 0.986 | 0.310 ($S_0$), 0.307 ($S_1$) |
| CNA−Ar | 0.641 | 0.469 | 0.555 | 0.308 |

| species | $A+B$ | $A-B$ | $A$ |
|---|---|---|---|
| CNA−(Ar)$_2$ | 0.654 | | 0.346 |
| CNA−(Ar)$_3$ | 0.528 | <0.035 | |

[a] In GHz. Averaged values for the $S_0$ and $S_1$ states otherwise noted. Estimated uncertainties are ±0.5%.

**3.1. Bare CNA.** Figure 2a shows an RCS-TRFD trace measured for the $S_1-S_0$ $0_0^0$ band of bare CNA located at 382.13 nm (in air).[14] The trace exhibits many transients with various line shapes in the entire time region. The most prominent one appears as a negative-going spike at ~810 ps, and there are also spikes with the same polarity at 2 and 3 times the time delay of the first one. By comparing simulated traces calculated with appropriate molecular structures (see section 4.1), they are assigned to *C*-type transients, which occur at times $t \approx n/(4C)$ ($n$ being an integer). Another series of recurrences are also identified as *A*-type transients, which appear with no definite polarity at $t \approx n/(4A)$. The transients with $n$ up to 8 are observed for this type. One sees that the second *C*-type transient is broad and that the third one is even split into a doublet. This splitting indicates that the *C* constants in the ground and excited states are different enough that the shift in the corresponding *C*-type recurrences exceeds the experimental line width of the transients. Thus the analysis on bare CNA cannot be performed by varying a single set of rotational constants, and both the $S_0$ and $S_1$ rotational coherences must be explicitly included. By matching the measured and simulated TRFD traces, we obtain the values for the *C* constants in the $S_1$ and $S_0$ states and the *A* constant common to the two states, as are listed in Table 1. In this analysis, the *B* constants are calculated from the planarity condition, i.e., $1/C = 1/A + 1/B$. The smaller *C* constant is assigned to the $S_1$ state, because the ($\pi$, $\pi^*$) electronic excitation leads to a slight enlargement in the aromatic rings. As is shown

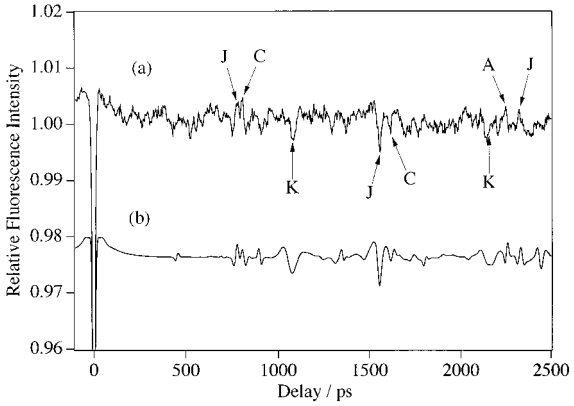


**Figure 3.** RCS traces of CNA−Ar. (a) Experimental TRFD trace recorded with the band at $\delta\nu = -48$ cm$^{-1}$. Features labeled with J's, K's, C's, and A's are assigned as *J*-, *K*-, *C*-, and *A*-type rotational coherence effects. (b) Simulated trace with the rotational constants taken as the values listed in Table 2.

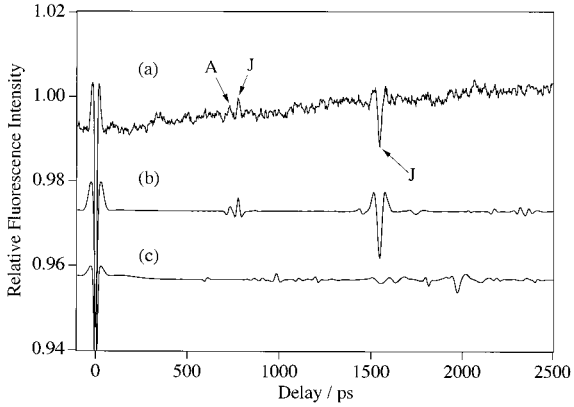


**Figure 4.** RCS traces of CNA−$(Ar)_2$. (a) Experimental TRFD trace recorded with the band at $\delta\nu = -91$ cm$^{-1}$. Features labeled with J's and A's are assigned as *J*- and *A*-type rotational coherence effects. (b) Simulated trace for the (1 + 1) isomer. The rotational constants are taken as the values listed in Table 2. (c) Simulated trace for the (2 + 0) isomer. The *A*, *B*, and *C* constants used are 0.415, 0.267, and 0.236 GHz, respectively. In the cluster, the *a* axis is along the *x* axis and the *c* axis is tilted by 22.5° from the *y* axis.

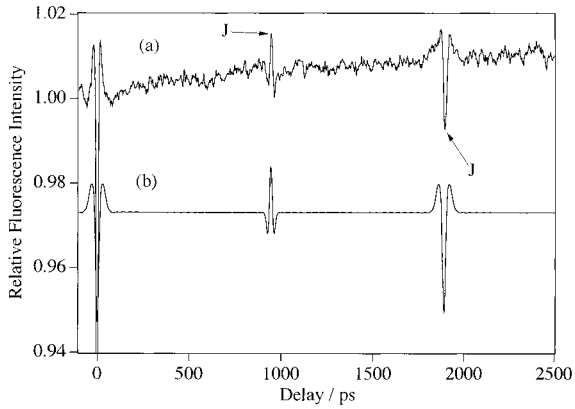


**Figure 5.** RCS traces of CNA−$(Ar)_3$. (a) Experimental TRFD trace recorded with the band at $\delta\nu = -130$ cm$^{-1}$. Features labeled with J's are assigned as *J*-type rotational coherence effects. (b) Simulated trace with the rotational constants taken as the values listed in Table 2.

in Figure 2b, the simulated RCS trace with the determined rotational constants reproduces most features in the observed one, including broad transients which do not correspond to any of the *J*-, *K*-, *A*-, or *C*-type recurrence.

**3.2. CNA−Ar.** Figure 3a shows an RCS-TRFD trace measured for the $S_1-S_0$ $0_0^0$ band of CNA−Ar, which is located at a shift ($\delta\nu$) of $-48$ cm$^{-1}$ from the corresponding monomer band.[45] There appears broad negative-going spike at ∼1080 ps, and another broad one with slightly smaller intensity is identified at almost double the time of the aforementioned peak. They are assigned to *K*-type transients, all occurring with negative polarity. Because the cluster is estimated as a near-prolate asymmetric top on the basis of its probable geometry, the spacing between the transients corresponds to $\sim 1/(4A - 2B - 2C)$. A sharp signal at ∼1560 ps is also prominent, which accompanies the other two positive-going peaks at one-half and three halves the time of the aforementioned peak. They are J-type transients, occurring with alternating polarity at $t \approx n/(2B + 2C)$. After simulated traces on the basis of the appropriate structure (see section 4.2) are compared, three transients are additionally assigned to the *C*- and *A*-type recurrences, as is indicated in Figure 3a. Owing to the existence of these four types of transients in the RCS trace, all of the three rotational constants can be determined independently from the experimental data. These constants, derived by the detailed comparison of the measured trace with those calculated while varying their values, are listed in Table 1. Uncertainties for the constants are estimated to be ±0.5%. The matchup between the observed (Figure 3a) and simulated (Figure 3b) traces is satisfactory, confirming the analysis.

**3.3. CNA−$(Ar)_2$.** Figure 4a shows an RCS-TRFD trace measured upon the excitation of the CNA−$(Ar)_2$ $0_0^0$ band at $\delta\nu = -91$ cm$^{-1}$.[45] It is much simpler than those for the monomer and CNA−Ar. Two transients, a positive-going one at 774 ps and a negative-going one at 1544 ps, are readily assigned as *J*-type on the basis of their equal spacing, their alternating polarity, and their relative magnitudes (the first being smaller than the second). The trace is characteristic of a near-prolate top, with the transition dipole moment along the *a* axis, or a near-oblate top, with the *c*-axis aligned transition dipole. The CNA−$(Ar)_2$ cluster is in the latter case (as is mentioned in 4.3), and thus, the *J*-type transient spacing corresponds to $\sim 1/(2A + 2B)$. In addition to these transients, the third one, which is positive going at 731 ps, is discernible in the trace. A comparison with those of simulated RCS traces (such as is shown in Figure 4b) indicates that this feature is the first *A*-type transient. Thus the $A + B$ and *A* constants have been determined as listed in Table 1.

**3.4. CNA−$(Ar)_3$.** Figure 5a shows an RCS-TRFD trace corresponding to the $\delta\nu = -130$ cm$^{-1}$ band assigned to CNA−$(Ar)_3$.[45] The clear, prominent transients at 951 and 1895 ps have the characteristics expected for *J*-type transients. As will be shown in section 4.4, the cluster is quite close to an oblate top, with the transition moment nearly along the *c* axis. Therefore, the observed transients directly fix the $A + B$ constant. A less precise measure of a second independent constant $A - B$ can also be obtained by the detailed comparison of the experimental trace with those simulated as a function of $A - B$. The determined values are listed in Table 1.

## 4. Analysis of Structures

In this section, we use the results of RCS reported above to ascertain effective zero-point geometrical parameters of CNA−$(Ar)_n$ ($n = 0-3$). In doing this, we make the usual assumption that the geometry of the CNA moiety does not change upon cluster formation. Note that in this work the rotational coherence effects observed for each species represent the unresolved contributions of ground- and excited-state coherences,[49] except for the *C*-type transients of bare CNA. Therefore, the structural

**TABLE 2: Structural Parameters of CNA−$(Ar)_n$ ($n = 1-3$) and Their Corresponding Rotational Constants**

| | $x^a$ | $y^a$ | $z^a$ | $A^b$ | $B^b$ | $C^b$ |
|---|---|---|---|---|---|---|
| CNA−Ar | 0.0 | (0.24/0.62) ± 0.2[c] | 3.46 ± 0.03 | 0.554 | 0.332 | 0.308 |
| CNA−$(Ar)_2$ | 0.0 | (0.16/0.70) ± 0.2[c] | 3.44 ± 0.03 | 0.346 | 0.308 | 0.244 |
| | 0.0 | (0.16/0.70) ± 0.2[c] | −3.44 ± 0.03 | | | |
| CNA−$(Ar)_3$ | 1.88 | 0.0 | 3.48 ± 0.04 | 0.265 | 0.263 | 0.181 |
| | −1.88 | 0.0 | 3.48 ± 0.04 | | | |
| | 0.0 | 0.24/0.62[c] | −3.46 | | | |

[a] Coordinates (in Å) of the Ar atoms in the CNA-fixed axis system defined in Figure 1. Values determined from the RCS-derived rotational constants (listed in Table 1) are indicated with estimated uncertainties. Others are fixed values. The coordinates of the first, second, and third atoms are on the corresponding lines. [b] Rotational constants (in GHz) calculated with the listed coordinates for the Ar atoms. [c] Two possible choices give the same rotational constants.

parameters determined from the present RCS-TRFD data represent averages of the parameters corresponding to the two states. In other words, they are identical for $S_1$ and $S_0$ within the quoted uncertainties. Throughout the analysis, the positions of the argon atoms are indicated with the CNA-fixed axis system shown in Figure 1.

**4.1. Bare CNA.** Before the structures of the CNA clusters with Ar atom(s) are analyzed, the structure of the CNA monomer itself must be considered. Crystal X-ray diffraction data on CNA have been reported, but the determined structure is substantially distorted from planarity.[52] Because the nonplanar geometry cannot be adopted as that of the CNA molecule in isolated conditions, its structure in the electronic ground state is assumed to be as follows. First, the crystal structure of anthracene[53] is invoked. Then, the hydrogen atom at the nine position of the anthracene is replaced with the cyano group, whose bond distances are taken from the crystal values of the CNA molecule.[52] This geometry concerning the −C≡N unit is essentially identical to that in benzonitrile.[24] The *A*, *B*, and *C* rotational constants for the structure are calculated to be: 0.988, 0.454, and 0.311 GHz, respectively, which agree well with the RCS-derived values for the electronic ground state ($A = 0.986$, $B = 0.452$, and $C = 0.310$ GHz). Now, if the carbon skeleton of the anthryl moiety is stretched by 1% along the *x* axis, the rotational constants *A*, *B*, and *C* become 0.988, 0.445, and 0.307 GHz, respectively, which agree with those of the electronic excited state (0.986, 0.446, and 0.307 GHz). Hereafter, in the structural analysis of the CNA−$(Ar)_n$ clusters, the geometry of the CNA moiety is assumed to have the averaged structure of those for $S_0$ and $S_1$ mentioned above.

**4.2. CNA−Ar.** The best candidate for the geometry of CNA−Ar is that similar to the 1:1 clusters of other tricyclic aromatics, e.g., anthracene[33] and fluorene,[26] in which the Ar atom is located above the central ring of the molecules. The rotational constants for the structure agree reasonably well with those determined by RCS, when the distance between Ar and the CNA plane is fixed at ∼3.4−3.6 Å, which is appropriate to aromatics−Ar. For a more detailed analysis, the experimentally determined rotational constants have been subjected to a least-squares fitting to derive the geometrical parameters. The cluster is assumed to be of $C_s$ symmetry, fixing the *x* coordinate of Ar to zero. There remain two independent parameters for characterizing the cluster geometry, and we chose the *y* and *z* coordinates of Ar in the CNA-fixed axis system as variables to be determined. The results are $y = (0.24 \text{ or } 0.62) \pm 0.07$ Å and $z = 3.457 \pm 0.004$ Å, where errors represent 1 standard deviation of the fit. These values are listed in Table 2 along with the calculated rotational constants evaluated for the fixed geometry. It is noted that the two values for *y* give the same rotational constants, because the moments of inertia of the cluster depend on the squares of the displacements of Ar from the CNA center of mass [located at $(x, y, z) = (0, 0.433, 0)$ in angstroms in the present coordinate system]. Thus, there are two possible geometries for CNA−Ar, as are displayed pictorially in Figure 6. To differentiate the two structures, it is necessary to attain the data on other isotopomer(s) in which the CNA center of mass is shifted from the original position. Unfortunately, any isotopic substituted species of CNA is difficult to obtain, leaving the ambiguity on the structure. In accordance with symmetry, the *a* axis is exactly aligned with the *x* axis, whereas the *b* axis is slightly off (∼9.6°) from the *y* axis for both of the geometries.

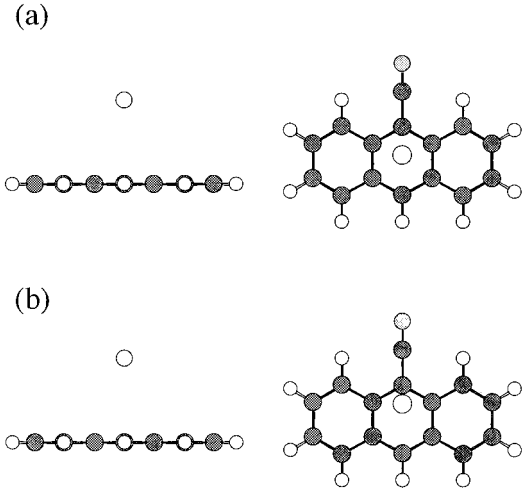


**Figure 6.** Two possible structures (left: side view, right: top view) of CNA−Ar determined by a least-squares fitting of the RCS-derived rotational constants. The CNA-fixed (*x*, *y*, *z*) coordinates (in Å) for the Ar atom are (a) (0, 0.24, 3.46) and (b) (0, 0.62, 3.46).

We have estimated the largest deviations from the geometry of Figure 6, while keeping consistent with the experimental data. We found that displacements of the Ar atom by ±0.4, ±0.2, and ±0.03 Å along the *x*, *y*, and *z* axes, respectively, yield structures which agree with the measured rotational constants within the experimental errors. These values are quoted in Table 2 as estimated uncertainties for the determined structural parameters.

**4.3. CNA−$(Ar)_2$.** As is mentioned in the Introduction, there are two possible bonding topologies for the CNA−$(Ar)_2$ cluster: the (1 + 1) isomer with Ar atoms on opposite sides of the CNA plane or the (2 + 0) isomer with both atoms on the same side of the substrate. The structures of the two isomers are presented in Figure 7. When we assume appropriate intermolecular distances (those between Ar and the CNA plane of ∼3.4−3.6 Å and that between the two contacting Ar atoms of ∼3.8 Å), the (1 + 1) isomer is a near-oblate top with the transition moment along the *c* axis, whereas the (2 + 0) isomer is a near-prolate top with the (almost) *c*-axis aligned transition moment. Thus, the former is consistent with the observed features of the experimentally derived RCS trace for CNA−$(Ar)_2$, but the latter is not. This correspondence is clearly indicated as simulated traces for the both candidates, as is shown in Figure 4b,c. These traces are drawn in the same scale, and it is apparent that the (2 + 0) isomer does not show RCS transients as prominently as the (1 + 1) isomer does. In particular, intervals of the *J*-type transients for the (2 + 0) isomer correspond to $\sim 1/(2B + 2C)$, which are too large (∼990 ps) to match those of the observed *J*-type transients.

Because the observed CNA−$(Ar)_2$ cluster is definitely assigned as the (1 + 1) form, its structural parameters are

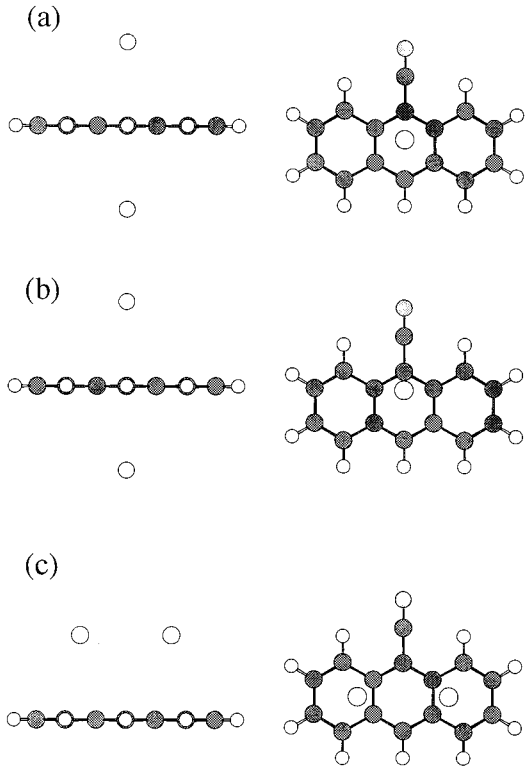


**Figure 7.** (a) and (b) Two possible structures of the (1 + 1) type CNA−$(Ar)_2$, which are consistent with the RCS-derived rotational constants. The CNA-fixed coordinates (in Å) for the two Ar atoms are (a) (0, 0.24, 3.46) and (0, 0.24, −3.46) and (b) (0, 0.62, 3.46) and (0, 0.62, −3.46). (c) Geometry of the (2 + 0) isomer of CNA−$(Ar)_2$. The coordinates for the Ar atoms are assumed as (1.88, 0, 3.48) and (−1.88, 0, 3.48).

evaluated from the experimentally determined rotational constants. Here we assume $C_{2v}$ symmetry for the cluster, in which two Ar atoms are at the reflective sites with respect to the CNA plane. Their *x* coordinates are accordingly zero. Then, there are two independent parameters to fix the cluster geometry, and we take the *y* and *z* coordinates of one Ar atom (for the other Ar, the corresponding values are *y* and −*z*, respectively). Because only two rotational constants, *A* and *A* + *B*, are available as experimental data, we directly derive the parameters from the constants. The determined values are listed in Table 2, along with the calculated rotational constants for the derived geometries. Uncertainties for the parameters are calculated from the estimated errors for the observed *A* and *A* + *B* constants, as are also listed in the table. As in the case of CNA−Ar, there are two possible values for *y* to reproduce the rotational constants. The corresponding two possible geometries are shown in Figure 7a,b. In accordance with symmetry, the *a*, *b*, and *c* axes of the cluster are exactly along the *x*, *z*, and *y* axes, respectively. As is listed in Table 2, the positions of the Ar atom(s) relative to the CNA plane are the same for the CNA−Ar and −$(Ar)_2$ clusters within the experimental uncertainties. This suggests that the local structure for an Ar atom on one side of the CNA plane is little influenced by the Ar atom that is located on the other side.

**4.4. CNA−$(Ar)_3$.** Here we assume the observed CNA−$(Ar)_3$ cluster as the (2 + 1) isomer, in which two Ar atoms are on the same side of the CNA plane and the other Ar is on the opposite side, as is shown in Figure 8, because it has been shown that the related cluster anthracene−$(Ar)_3$ has this type of geometry.[33] With appropriate intermolecular distances, this isomer is quite close to an oblate symmetric top with the transition moment

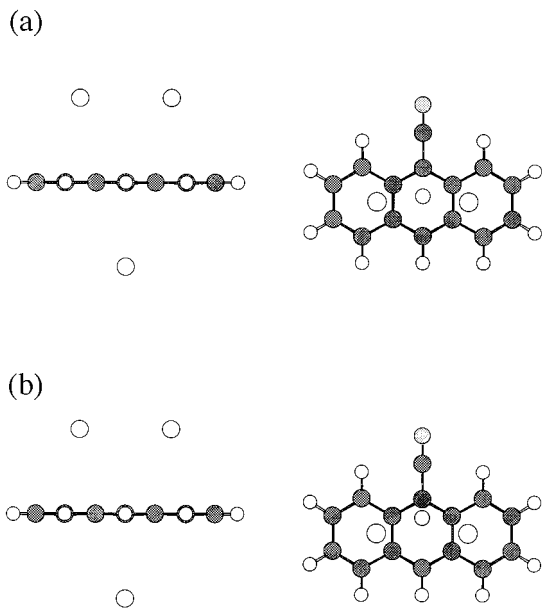


**Figure 8.** Two possible structures of CNA−$(Ar)_3$, which are consistent with the RCS-derived rotational constants. The coordinates (in Å) for the Ar atoms are (a) (1.88, 0, 3.48), (−1.88, 0, 3.48), and (0, 0.24, −3.46) and (b) (1.88, 0, 3.48), (−1.88, 0, 3.48), and (0, 0.62, −3.46).

almost along the *c* axis and, thus, is consistent with the above-mentioned features of the observed RCS trace of the species. The simulated trace for the (2 + 1) geometry reproduces the observed one quite well, as is mentioned later, which confirms the structural assignment.

Having identified its gross structure, we deduce quantitative geometrical parameters for CNA−$(Ar)_3$ from the RCS data. In this analysis, the species is assumed to be of $C_s$ symmetry. Even with this symmetry constraint, there are five parameters to fix an unambiguous geometry of the species, whereas the experimentally available data are only two (the *A* + *B* and less precise *A* − *B* constants). Thus we have to make some assumptions on the parameters as follows. First, the distance between the two Ar atoms on the same side is fixed at the equilibrium internuclear distance of the gas-phase argon dimer (3.76 Å).[54] Second, the position of the third Ar atom is fixed to that of CNA−Ar. This assumption is rationalized by the above-mentioned finding that the local structure for Ar on the CNA plane is identical to each other for CNA−Ar and −$(Ar)_2$. From the *A* + *B* and *A* − *B* constants, the distance of the Ar dimer from the CNA plane was obtained to be 3.48 Å, for which the uncertainty was evaluated as ±0.04 Å from the estimated errors for the rotational constants. The two possible values for *y* of the "single" Ar atom give the same results within the quoted uncertainty. It is found that the *y* coordinate of the Ar dimer has a small influence on the rotational constants. In particular, *A* + *B* remains almost constant when the value is in the range from −0.4 to +1.2 Å. Thus, we finally assume its value as zero. The distance between the two Ar atoms in the dimer unit has been checked to have also little effect on the rotational constants in the range of 3.76 ± 0.22 Å. The results are summarized in Table 2, with the calculated rotational constants for the determined structure. Note that the *A* and *B* constants differ from each other only by ∼2 MHz. The *a* axis of the cluster is along the *x* axis, and the *c* axis is tilted from the *y* axis by ∼8.5°. The simulated RCS trace for the determined structure is shown in Figure 5b, which agrees well with the observed one (Figure 5a).

## 5. Discussion

**5.1. Two Possible Conformations for $n = 2$: (2 + 0) vs (1 + 1) Isomers.** The molecular structures of the CNA−$(Ar)_n$ ($n$ = 1−3) clusters established as above show similarity and difference to those of anthracene−$(Ar)_n$. For the $n = 1$ and 3 clusters, the conformations of both of the series are the same [(1 + 0) and (2 + 1) types, respectively], but the dominant form of CNA−$(Ar)_2$ has the (1 + 1)-type geometry, in contrast to its analogue, anthracene−$(Ar)_2$, which has been identified as the (2 + 0) type.[33] Because relative populations of (meta)-stable conformers in supersonic expansions should be mainly controlled by their energetics, the difference in the dominant conformations for $n = 2$ implies that the stabilities for the (2 + 0) and (1 + 1) types are quite close to each other for clusters of anthracene and its derivatives. A small change in the intermolecular interactions by the introduction of substituted group(s) may invert the energy ordering for the two conformations. This situation is demonstrated as follows by model calculations using pairwise atom−atom additive potentials, which have been extensively adopted to estimate the geometry, intermolecular vibrations, and internal dynamics of aromatic−(rare gas)$_n$ clusters.[4,5,7−11,18]

For anthracene−$(Ar)_2$, Uridat et al. have calculated that the (2 + 0) form is more stable by ∼20 cm$^{-1}$ than the (1 + 1) form with their parameters for Lennard-Jones (LJ) potentials.[11] The relative stabilities are essentially the same when using the different set of parameters,[9] though the absolute binding energies ($D_e$'s) show considerable changes. These calculations are in accord with the experimental observation. In the case of CNA−$(Ar)_2$, calculations show a larger dependence on the potential parameters. The parameters of Uridat et al.[11] give the (2 + 0) form as more stable by 14 cm$^{-1}$ than the (1 + 1) form ($D_e$ = 1019 and 1005 cm$^{-1}$, respectively). The difference between them is only 2 cm$^{-1}$ when adopting the parameters of Troxler and Leutwyler[9] [$D_e$ = 936 and 934 cm$^{-1}$ for (2 + 0) and (1 + 1)]. For both of the calculations, the Ar−N interaction is taken from the evaluation by Ohline et al.[40] The pairwise potentials effectively represent the dispersion and exchange−repulsion interactions for Ar−Ar and Ar−aromatics, and the additional stabilization by the dispersion concerning the substituted cyano group reduces the energy difference between the two conformers. However, this level of approximation still estimates the most stable form for CNA−$(Ar)_2$ as the (2 + 0) isomer.

We further consider the induction interaction between the polarizable Ar atoms and the aromatic molecule with nonuniform charge distribution.[3] The electric fields at the points of Ar are evaluated by distributing point charges at each of the atoms in the CNA molecule in accordance with the B3LYP/6-31G(d,p) calculation, and the Ar atoms are regarded as point polarizabilities ($\alpha = 1.64$ Å$^3$). The contributions of the induction to the binding energies are 7 and 16 cm$^{-1}$ for the (2 + 0) and (1 + 1) forms, respectively. Their absolute values are quite small compared to those of the total energies, but their difference is crucial. The additional stability for (1 + 1) relative to (2 + 0) makes for the inversion of the energy ordering for the two conformations, when the preferable set of the LJ parameters is adopted.

In addition to the two-body intermolecular interactions considered above, three-body effects should be taken into account. These terms are much smaller than those of the total binding energies, but may cause a significant change in the relative stabilities for the two isomers.[4,7] Indeed, Leutwyler has estimated that the (2 + 0) isomer of perylene−$(Ar)_2$ is *de*stabilized by 10 cm$^{-1}$, whereas the effect on the (1 + 1) isomer is negligible.[4] This finding is rationalized because the dominant term is the Axilrod−Teller−Muto type triple-dipole dispersion[55] in this case, which is positive when the three constituents are in contact with each other because of its angular dependence and inversely proportional to the cubes of the distances between each of the two units. Consequently, the (2 + 0) form becomes less stable (by a small amount), whereas the (1 + 1) form is little affected because of the larger Ar−Ar separation. This three-body interaction will contribute to the clusters of anthracene and CNA in a similar manner, giving a further preference to the (1 + 1) isomer. In total, it is reasonable to estimate that the (1 + 1) form is slightly more stable than the (2 + 0) form in the case of CNA−$(Ar)_2$, which is now consistent with the present observation.

We next discuss the possibility for detecting the less stable forms of the $n = 2$ clusters for anthracene and CNA. In accordance with the above-mentioned calculations, the energy differences between the (2 + 0) and (1 + 1) forms are ≤20 cm$^{-1}$, which are not much larger than the internal energies deposited in the clusters even under adiabatically cooled conditions. The rotational temperature is estimated as ∼5 K, and the effective temperature for isomerization must be higher than this. If we assume a temperature of 10 K, the relative populations for the less stable isomers are more than 5% of those of the observed (most stable) conformers. Thus the detection of the species may not be a tough demand for experiments performed nowadays with sensitive detection methods. However, there has been no definite identification of the (1 + 1) isomer for anthracene−$(Ar)_2$. The band at $\delta\nu$ = −87 cm$^{-1}$ previously assigned to an isomer[5] has been confirmed as that of anthracene−$H_2O$,[11] and the broad feature centered at $\delta\nu \sim -84$ cm$^{-1}$ is now considered to be hot bands of the most stable (2 + 0) isomer.[11] In the case of CNA−$(Ar)_2$, we have observed another band at $\delta\nu = -82$ cm$^{-1}$ with $^1/_4$ the intensity of that of the (1 + 1) origin. We have performed an RCS measurement by monitoring the additional band, but no appreciable RCS transients can be observed at $\Delta t > 0$, suffered by the insufficient S/N ratio due mainly to the smaller band intensity. The failure in observing the RCS transients is not inconsistent with the possible assignment to the (2 + 0) isomer, because the transients for the isomer may be much less prominent than those of the (1 + 1) isomer, as shown in Figure 4c. No conclusive identification can be made at present, and further information should be provided by other experimental methods, e.g., mass-selective resonance-enhanced ionization and spectral hole-burning.

**5.2. Comparison of the Geometrical Parameters.** A number of aromatic−Ar clusters have been studied with the experimental methods with rotational resolution, and their geometrical parameters have been determined.[19−35] The reported values of the distances between the aromatic molecular plane and the Ar atom are summarized in Table 3. The present result on CNA−Ar is also listed in the table. The most remarkable trend is that all of the values in the clusters of polycyclic aromatics fall in a relatively narrow range of 3.42−3.46 Å (as averages for $S_0$ and $S_1$). On the other hand, those for monocyclic aromatics are slightly larger (3.50−3.58 Å in the $S_0$ state) except for furan−Ar and *s*-tetrazine−Ar.[19,25] These small changes from mono- to polycyclic aromatics may originate partly from the slightly stronger dispersion attraction from atoms in the outer rings in the latter species. The model calculations with the LJ potentials used in the preceding section predict the changes in the correct direction, but they are not always quantitatively good. Apparently, changes in the $\pi$-electron density in the aromatic ring on

**TABLE 3: Distances from the Molecular Plane to Ar in Aromatic−Ar Clusters**

| molecule | $z$ ($S_0$)[a,b] | $z$ ($S_1$)[a,c] | $z$ (ave)[a] | ref |
|---|---|---|---|---|
| benzene | 3.581 | 3.521[d] | 3.551 | 22, 27, 39 |
| benzonitrile | 3.545 | 3.48 | 3.51 | 24, 30 |
| aniline | 3.508 | 3.448 | 3.478 | 29 |
| fluorobenzene | 3.553 | | | 23 |
| *p*-difluorobenzene | 3.55 | 3.49 | 3.52 | 28, 34 |
| pyridine | 3.539 | | | 20 |
| *s*-tetrazine | 3.429 | 3.40 | 3.415 | 25 |
| furan | 3.479 | | | 19 |
| pyrrole | 3.537 | | | 21 |
| indole | 3.435 | 3.400 | 3.417 | 31 |
| anthracene | | | 3.43 | 33 |
| CNA | | | 3.46 | this work |
| 9,10-dichloroanthracene | | | 3.42 | 33 |
| fluorene | | | 3.42 | 26 |
| tetracene | | | 3.43 | 33 |
| perylene | | | 3.42 | 32 |

[a] Distance from the aromatic molecular plane to the Ar atom on it. [b] Values evaluated from the rotational constants for the $S_0$ vibrational ground state. [c] Values evaluated from the rotational constants for the $S_1$ $0^0$ state otherwise noted. [d] Value for the $6^1$ vibronic state.

which Ar lies should also be important, and this requires species- and site-dependent parametrization for IPSs.

In contrast to anthracene−Ar, CNA−Ar does not have to locate its Ar atom on the center of the central aromatic ring, because the symmetry of the substrate is lower than that of anthracene, because of cyano-group substitution. The present study has shown that the Ar atom in it is shifted *toward* the cyano group by 0.2 or 0.6 Å. Because the measurement only on a single isotopic species cannot differentiate the two possibilities, we will consult the results on related aromatic clusters to find out which is the more preferable. For benzonitrile−Ar,[24] aniline−Ar,[29] and pyridine−Ar,[20] two isotopic variants have been studied to determine the cluster structures. It has been shown that the Ar atom is shifted from the center of the six-membered aromatic ring toward the functional group (−CN, $-NH_2$, or aza nitrogen), as in CNA−Ar. The shifts have been determined to be 0.24, 0.29, and 0.24 Å, respectively, in the $S_0$ state. These are quite close to the smaller value in CNA−Ar, and thus the shift is most likely 0.2 Å. The model potential calculation has estimated the shift to be ∼0.15−0.20 Å, which also supports the conclusion. The calculated shift is determined mainly by the change in the dispersion + exchange−repulsion terms because of the cyano-group substitution, but the induction interaction also contributes ∼20−25% to the total shift.

**5.3. Additivity Relations for (1 + 0) and (1 + 1) Clusters.** The present study has shown that the positions of the Ar atoms relative to the aromatic plane are the same in the (1 + 0)-type CNA−Ar and the (1 + 1)-type CNA−$(Ar)_2$ within the experimental uncertainties. It is simply because the interaction between the two Ar atoms located in the opposite sides of the substrate is too small to make a measurable structural change. In other words, the geometry on one side is independent of that on the other side, and thus the structure of the ($m$ + $n$)-type cluster must be represented as a simple addition of the ($m$ + 0)- and (0 + $n$)-type structures. This "structural additivity" has also been confirmed by the studies on the (1 + 0)- and (1 + 1)-type clusters of *s*-tetrazine−$(Ar)_{1,2}$,[25] benzene−$(Ar)_{1,2}$,[22,27,39] pyridine−$(Ar)_{1,2}$,[20,37] furan−$(Ar)_{1,2}$,[19,36] perylene−$(Ar)_{1,2}$,[32] and fluorene−$(Ar)_{1,2}$.[26,42]

Correlating to the structural additivity, we next examine the additivity relation in the $S_1$−$S_0$ spectral shifts. The value for CNA−$(Ar)_2$ is $\delta\nu(n = 2) = 1.90\delta\nu(n = 1)$, nearly equal to twice the CNA−Ar value. Therefore, the additivity relation approximately holds for the species, but there is a sizable deviation [$\delta\nu(n = 2) - 2\delta\nu(n = 1) = 5$ cm$^{-1}$]. The absolute value of the deviation is almost identical to that of fluorene−$(Ar)_{1,2}$[26,42] but notably larger than those for the clusters with *s*-tetrazine,[25] benzene,[27,39] carbazole,[8] and perylene.[4] At present, the origin of the deviation is uncertain. The second-order perturbation theory considering the long-range attractive solute−solvent interactions predicts that the spectral shifts induced by different solvent molecules are strictly additive.[6] This prediction assumes that the structure concerning one side are exactly the same irrespective to the coordination on the other side. A more elaborate theory must be necessary that considers structural changes which are too small to be detected experimentally. In addition, other minor effects, e.g., three-body interaction due to induction, may contribute to some extent.

## 6. Conclusion

We have presented the structural characterization of the CNA−$(Ar)_n$ ($n$ = 1−3) clusters on the basis of the experimental attainments by RCS. The gross structures for $n$ = 1−3 have been determined as (1 + 0), (1 + 1), and (2 + 1) types, respectively, suggesting the relative preference for central binding of Ar atoms to CNA. In particular, the conformation for CNA−$(Ar)_2$ is rather similar to those for carbazole−$(Ar)_2$ and fluorene−$(Ar)_2$[40−42] but is in contrast to that for anthracene−$(Ar)_2$, which has been identified as the (2 + 0) type.[33] Model potential calculations predict the binding energies of the (1 + 1) and (2 + 0) forms in close proximity, and the former conformation will be preferable because of the slightly stronger dispersion and induction interactions provided by the cyano substitution. Such a subtle balance in relative stabilities for one- and two-sided conformations will be a common feature in clusters of other substituted anthracenes complexed with rare-gas atoms, and the coexistence of the two isomers can be observed as in the case of perylene−$(Ar)_2$.[4,32]

**Acknowledgment.** The present work has been supported by Grants-in-Aid (Nos. 08454177 and 10440172) from the Ministry of Education, Science, Culture, and Sports of Japan. Additional support has been provided from Japan Science and Technology Corporation (JST). Y.O. thanks the Mitsubishi Chemical Foundation, the Japan Securities Scholarship Foundation, and the Asahi Glass Foundation for financial support.

## References and Notes

(1) Amirav, A.; Even, U.; Jortner, J. *J. Chem. Phys.* **1981**, *75*, 2489.
(2) Leutwyler, S.; Even, U.; Jortner, J. *J. Chem. Phys.* **1983**, *79*, 5769.
(3) Amirav, A.; Even, U.; Jortner, J.; Dick, B. *Mol. Phys.* **1983**, *49*, 899.
(4) Leutwyler, S. *J. Chem. Phys.* **1984**, *81*, 5480.
(5) Henke, W. E.; Yu, W.; Selzle, H. L.; Schlag, E. W.; Wutz, D.; Lin, S. H. *Chem. Phys.* **1985**, *92*, 187.
(6) Shalev, E.; Ben-Horin, N.; Even, U.; Jortner, J. *J. Chem. Phys.* **1991**, *95*, 3147. Shalev, E.; Ben-Horin, N.; Jortner, J. *J. Chem. Phys.* **1992**, *96*, 1848.
(7) Leutwyler, S.; Jortner, J. *J. Phys. Chem.* **1987**, *91*, 5558.
(8) Leutwyler, S.; Bösiger, J. *Chem. Rev.* **1990**, *90*, 489.
(9) Troxler, T.; Leutwyler, S. *J. Chem. Phys.* **1993**, *99*, 4363.
(10) Schmidt, M.; Le Calvé, J.; Mons, M. *J. Chem. Phys.* **1993**, *98*, 6102.
(11) Uridat, D.; Brenner, V.; Dimicoli, I.; Le Calvé, J.; Millié, P.; Mons, M.; Piuzzi, F. *Chem. Phys.* **1998**, *239*, 151.
(12) Bernstein, E. R. In *Chemical Reactions in Clusters*; Bernsein, E. R., Ed.; Oxford University Press: New York, 1996; Chapter 5 and references sited therein.
(13) Topp, M. R. In *Jet Spectroscopy and Molecular Dynamics*; Hollas, J. M., Phillips, D., Eds.; Chapman and Hall: London, 1995; Chapter 8.
(14) Amirav, A.; Horwitz, C.; Jortner, J. *J. Chem. Phys.* **1988**, *88*, 3092.

(15) Brupbacher, Th.; Makarewicz, J.; Bauder, A. *J. Chem. Phys.* **1994**, *101*, 9736.
(16) Bludský, O.; Špirko, V.; Hrouda, V.; Hobza, P. *Chem. Phys. Lett.* **1992**, *196*, 410.
(17) Koch, H.; Fernández, B.; Makarewicz, J. *J. Chem. Phys.* **1999**, *111*, 198. Fernández, B.; Koch, H.; Makarewicz, J. *J. Chem. Phys.* **1999**, *111*, 5922.
(18) Ondrechen, M. J.; Berkovitch-Yellin, Z.; Jortner, J. *J. Am. Chem. Soc.* **1981**, *103*, 6586.
(19) Kukolich, S. G. *J. Am. Chem. Soc.* **1983**, *105*, 2207.
(20) Klots, T. D.; Emilsson, T.; Ruoff, R. S.; Gutowsky, H. S. *J. Phys. Chem.* **1989**, *93*, 1255.
(21) Bohn, R. K.; Hillig, K. W., II; Kuczkowski, R. L. *J. Phys. Chem.* **1989**, *93*, 3456.
(22) Brupbacher, Th.; Bauder, A. *Chem. Phys. Lett.* **1990**, *173*, 435.
(23) Stahl, W.; Grabow, J.-U. *Z. Naturforsch.* **1992**, *47A*, 681.
(24) Dahmen, U.; Stahl, W.; Dreizler, H. *Ber. Bunsen-Ges. Phys. Chem.* **1994**, *98*, 970.
(25) Haynam, C. A.; Brumbaugh, D. V.; Levy, D. H. *J. Chem. Phys.* **1984**, *80*, 2256.
(26) Meerts, W. L.; Majewski, W. A.; van Herpen, W. M. *Can. J. Phys.* **1984**, *62*, 1293.
(27) Weber, Th.; von Bargen, A.; Riedle, E.; Neusser, H. J. *J. Chem. Phys.* **1990**, *92*, 90.
(28) Sussmann, R.; Neuhauser, R.; Neusser, H. J. *Can. J. Phys.* **1994**, *72*, 1179.
(29) Sinclair, W. E.; Pratt, D. W. *J. Chem. Phys.* **1996**, *105*, 7942.
(30) Helm, R. M.; Vogel, H.-P.; Neusser, H. J. *Chem. Phys. Lett.* **1997**, *270*, 285.
(31) Korter, T. M.; Küpper, J.; Pratt, D. W. *J. Chem. Phys.* **1999**, *111*, 3946.
(32) Ohline, S. M.; Joireman, P. W.; Connell, L. L.; Felker, P. M. *Chem. Phys. Lett.* **1992**, *191*, 362.
(33) Ohline, S. M.; Rosmascan, J.; Felker, P. M. *J. Phys. Chem.* **1995**, *99*, 7311.
(34) Riehn, C.; Weichert, A.; Zimmermann, M.; Brutschy, B. *Chem. Phys. Lett.* **1999**, *299*, 103.
(35) Fujiwara, T.; Fujimura, Y.; Kajimoto, O. *J. Chem. Phys.* **2000**, *113*, 11109.
(36) Spycher, R. M.; King, P. M.; Bauder, A. *Chem. Phys. Lett.* **1992**, *191*, 102. Spycher, R. M.; Hausherr-Primo, L.; Grassi, G.; Bauder, A. *J. Mol. Struct.* **1995**, *351*, 7.
(37) Spycher, R. M.; Petitprez, D.; Bettens, F. L.; Bauder, A. *J. Phys. Chem.* **1994**, *98*, 11863.
(38) Schimidt, M.; Mons, M.; Le Calvé, J.; *Chem. Phys. Lett.* **1991**, *177*, 371. Mons, M.; Courty, A.; Schmidt, M.; Le Calvé, J.; Piuzzi, F.; Dimicoli, I. *J. Chem. Phys.* **1997**, *106*, 1676.
(39) Weber, Th.; Neusser, H. J. *J. Chem. Phys.* **1991**, *94*, 7689.
(40) Ohline, S. M.; Connell, L. L.; Joireman, P. W.; Venturo, V. A.; Felker, P. M. *Chem. Phys. Lett.* **1992**, *193*, 335.
(41) Su$\beta$mann, R.; Neusser, H. J. *Chem. Phys. Lett.* **1994**, *221*, 46.
(42) Su$\beta$mann, R.; Zitt, U.; Neusser, H. J. *J. Chem. Phys.* **1994**, *101*, 9257.
(43) Felker, P. M. *J. Phys. Chem.* **1992**, *96*, 7844.
(44) Amirav, A.; Jortner, J.; Okajima, S.; Lim, E. C. *Chem. Phys. Lett.* **1986**, *126*, 487.
(45) Hirayama, S.; Shobatake, K.; Tabayashi, K. *Chem. Phys. Lett.* **1985**, *121*, 228.
(46) Bakhshiev, N. G. *Opt. Spektrosk.* **1992**, *72*, 203.
(47) Côté, M. J.; Kauffman, J. F.; Smith, P. G.; McDonald, J. D. *J. Chem. Phys.* **1989**, *90*, 2865. Kauffman, J. F.; Côté, M. J.; Smith, P. G.; McDonald, J. D. *J. Chem. Phys.* **1989**, *90*, 2874.
(48) Felker, P. M.; Zewail, A. H. *J. Chem. Phys.* **1987**, *86*, 2460.
(49) Hartland, G. V.; Connell, L. L.; Felker, P. M. *J. Chem. Phys.* **1991**, *94*, 7649.
(50) Felker, P. M.; Zewail, A. H. In *Femtosecond Chemistry*; Manz, J., Wöste, L., Eds.; VCH: Weinheim, Germany, 1995; Vol. I, Chapter 5.
(51) Macfarlane, R. M.; Philpott, M. R. *Chem. Phys. Lett.* **1976**, *41*, 33.
(52) Rabaud, H.; Clastre, J. *Acta Crystallogr.* **1959**, *12*, 911.
(53) Cruickshank, D. W. J.; Sparks, R. A. *Proc. R. Soc. London, Ser. A* **1960**, *258*, 270.
(54) Herman, P. R.; LaRocque, P. E.; Stoicheff, B. P. *J. Chem. Phys.* **1988**, *89*, 4535.
(55) Stone, A. J. *The Theory of Intermolecular Forces*; Oxford University Press: Oxford, U.K., 1996.